



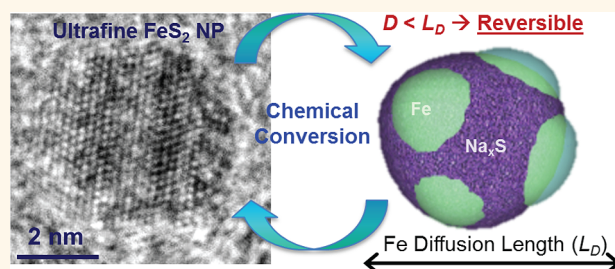
# Ultrafine Iron Pyrite ( $\text{FeS}_2$ ) Nanocrystals Improve Sodium–Sulfur and Lithium–Sulfur Conversion Reactions for Efficient Batteries

Anna Douglas,<sup>†,‡</sup> Rachel Carter,<sup>‡</sup> Landon Oakes,<sup>†,‡</sup> Keith Share,<sup>†,‡</sup> Adam P. Cohn,<sup>‡</sup> and Cary L. Pint<sup>\*,†,‡,§</sup>

<sup>†</sup>Interdisciplinary Materials Science Program and <sup>‡</sup>Department of Mechanical Engineering, Vanderbilt University, Nashville, Tennessee 37235, United States

<sup>§</sup>Vanderbilt Institute of Nanoscale Science and Engineering, Nashville, Tennessee 37235, United States

**ABSTRACT** Nanocrystals with quantum-confined length scales are often considered impractical for metal-ion battery electrodes due to the dominance of solid-electrolyte interphase (SEI) layer effects on the measured storage properties. Here we demonstrate that ultrafine sizes ( $\sim 4.5$  nm, average) of iron pyrite, or  $\text{FeS}_2$ , nanoparticles are advantageous to sustain reversible conversion reactions in sodium ion and lithium ion batteries. This is attributed to a nanoparticle size comparable to or smaller than the diffusion length of Fe during cation exchange, yielding thermodynamically reversible nanodomains of converted Fe metal and  $\text{Na}_x\text{S}$  or  $\text{Li}_x\text{S}$  conversion products. This is compared to bulk-like electrode materials, where kinetic and thermodynamic limitations of surface-nucleated conversion products inhibit successive conversion cycles. Reversible capacities over 500 and 600 mAh/g for sodium and lithium storage are observed for ultrafine nanoparticles, with improved cycling and rate capability. Unlike alloying or intercalation processes, where SEI effects limit the performance of ultrafine nanoparticles, our work highlights the benefit of quantum dot length-scale nanocrystal electrodes for nanoscale metal sulfide compounds that store energy through chemical conversion reactions.



**KEYWORDS:** iron pyrite ·  $\text{FeS}_2$  nanoparticles · chemical transformations · quantum dots · sodium sulfur · lithium sulfur · batteries

Over the course of the past decade, nanostructured materials have been widely used in energy storage and conversion electrodes to improve and optimize chemical storage processes.<sup>1–3</sup> Among the numerous advantages that nanostructured materials bring is the capability to engineer the size and shape of active storage building blocks to balance chemical kinetics of metal-ion intercalation reactions, yielding improved utility of active material,<sup>4–6</sup> less mechanical pulverization during cycling,<sup>7,8</sup> and better power capability.<sup>6,9</sup> However, it is not evident that these benefits scale down to nanostructures exhibiting length scales that lead to quantum confinement phenomena, such as quantum dots, where the particle size is comparable to the Bohr radius. Many of the most studied nanostructured materials for metal-ion batteries, such as silicon,<sup>10–13</sup> exhibit alloying or intercalation reactions

where the metal ions shuttle through a solid-electrolyte interphase (SEI) layer to store charge within the interior of the storage material. In these materials, reports have emphasized the detrimental effect of ultrafine nanoscale materials due to the dominance of the SEI layer on inhibiting reversible storage.<sup>14,15</sup> In the particular case of silicon, researchers have emphasized that SEI layer growth upon cycling in ultrasmall nanostructures can deactivate the active storage material, leading to lower capacity and shorter cycling lifetimes than larger nanoparticles.<sup>14</sup> Similar observations have been made with other intercalation or alloying storage materials as well, including antimony and tin nanocrystals, indicating that nanostructures that are too small may not be advantageous for metal-ion storage.<sup>16,17</sup> Recent work by He *et al.* shows the same trend for antimony that has been previously observed for silicon, where a nanocrystal

\* Address correspondence to cary.l.pint@vanderbilt.edu.

Received for review July 28, 2015 and accepted November 3, 2015.

Published online November 03, 2015  
10.1021/acsnano.5b04700

© 2015 American Chemical Society

size of 20 nm greatly outperforms those of 10 nm and bulk powder in terms of capacity, rate capability, and reversible cycling.<sup>16</sup>

In contrast to intercalation or alloying reactions, where metal atoms are reversibly shuttled in and out of a host lattice, conversion reactions involve the chemical transformation of one or more of the atomic species into a host lattice to form a new compound.<sup>18</sup> An example of this is the conversion of a metal disulfide,  $MS_2$ , into a conversion product involving metallic domains (M) and  $Na_2S$  or  $Li_2S$  compounds that can be reversibly formed.<sup>19</sup> Ultrafine nanoparticles ( $\sim 2\text{--}10\text{ nm}$ ) have been assessed for their capability to reversibly store charge through conversion reactions, including  $ZnO$ ,<sup>20</sup>  $SnO_2$ ,<sup>21</sup>  $CoO$ ,<sup>22</sup> and  $Co_3O_4$ ,<sup>23</sup> even though reasoning for why this differs from that observed in nonconversion reactions has not been identified or discussed.

In this spirit, the metal sulfides, which exhibit conversion reactions with lithium or sodium metal atoms, have been at the forefront of both fundamental and applied research in battery systems. Recent work by McDowell *et al.* has demonstrated lithium conversion reactions in metal sulfides to be dictated by the crystal structure of the host lattice as well as the diffusion length of metals during cation exchange to form  $Li_2S$  products.<sup>19</sup> As Cu (in  $Cu_2S$ ) exhibits long diffusion lengths, Fe (in  $FeS_2$ ) is limited to shorter diffusion lengths ( $L_D = 10^{-17}\text{ cm}^2\text{ s}^{-1}$  at 100 °C or  $\sim 10^{-18}\text{ cm}^2\text{ s}^{-1}$  at room temperature<sup>24</sup>) still inaccessible by most nanostructures. Thus, rational approaches to nanostructuring electrode materials can strongly impact the kinetics and thermodynamics of cation-exchange chemical storage transformations. Whereas most studies on metal sulfides are focused on the transition metal dichalcogenides,<sup>19,25,26</sup>  $FeS_2$  (cubic pyrite, “fool’s gold”) is a highly promising material that has not been widely studied for secondary battery systems.  $FeS_2$  is particularly attractive for energy storage technology due to its earth abundance, low toxicity, and low raw material cost.<sup>25,27</sup> As  $FeS_2$  is a common byproduct of coal production, it has been a stable, low-cost cathode material employed in off-the-shelf commercial lithium primary battery technology. Only recently has iron pyrite been investigated for secondary lithium ion batteries owing to a high theoretical capacity of 894 mAh/g<sup>28</sup> that comes from the storage of four lithium ions per  $FeS_2$  via a conversion reaction to Fe and  $Li_2S$ .<sup>29,30</sup> Studies have also recently shown that iron pyrite is a suitable material in a rechargeable sodium ion battery<sup>31,32</sup> and that the sodium undergoes the same conversion reaction to form Fe and  $Na_2S$ .<sup>33,34</sup> The conversion reaction within both sodium and lithium devices using pyrite leads to rapid degradation of active bulk storage material,<sup>35,36</sup> which has been improved by nanostructuring into nanocubes<sup>5</sup> and nanowires<sup>6</sup> with features greater than 50 nm.

In this work we explore the sodium and lithium conversion of ultrafine  $FeS_2$  nanoparticles, with a tight size distribution centered around  $\sim 4.5\text{ nm}$ , which is in the size regime where strong quantum confinement effects are observed.<sup>37</sup> Compared to nonconversion storage processes, we identify the ultrafine character of the nanoparticles to have a *beneficial* role in storage of sodium and lithium. This is due to ultrafine nanoparticles having a size comparable to the diffusion length of iron during a conversion reaction, leading to reversible and efficient cation exchange, a feature that is inhibited in larger nanocrystals or bulk materials. This “pins” conversion products to localized nanodomains, stabilized by the poor diffusion kinetics of Fe during cation exchange, and poses a synergy between  $FeS_2$ , one of the most stable and earth abundant battery materials, and ultrafine “quantum dot” nanoparticles.

## RESULTS AND DISCUSSION

To date, there have been few works performed on ultrafine nanoparticles for energy storage, and despite the promise anticipated for such materials, there has yet to be both fundamental and applied advances for quantum dot, or generally quantum-confined nanocrystal scale materials, in batteries. In this study, our focus is on the use of  $FeS_2$  due to the extensive use of  $FeS_2$  in commercial lithium primary battery applications. The combination of  $FeS_2$  materials with sodium-containing electrodes represents a realizable and cost-effective platform that captures the cost/performance promise of sodium–sulfur batteries<sup>38</sup> while simultaneously overcoming the operation limitations of such systems. To approach this effort, we focused on the wet chemical synthesis of  $FeS_2$  nanoparticles at sub-10 nm length scales through addition of aqueous sodium thiosulfate pentahydrate salts added dropwise into solutions containing iron(II) chloride tetrahydrate and thioglycolic acid.<sup>39</sup> This led to the formation of crystalline  $FeS_2$  nanoparticles with diameters between 2 and 9 nm. Transmission electron microscopy (TEM) and corresponding fast Fourier transform (FFT) show the crystalline and ultrafine nature of the nanoparticles (Figure 1a). TEM and FFT indicate a measured lattice spacing of 2.7 Å, which is consistent with the (200) plane of iron pyrite.<sup>5</sup> ImageJ image analysis software was used to assess the size distributions of nanoparticles evident in multiple TEM images (Figure 1b)<sup>40</sup> to obtain a log-normal distribution of nanoparticles with sizes between 2 and 9 nm and an average diameter near  $\sim 4.5\text{ nm}$ . This size range of  $FeS_2$  nanoparticles is comparable with the Bohr radius ( $\sim 1.3\text{ nm}$ ) and hence correlates with the size regime in which quantum confinement effects are observed,<sup>37</sup> evidenced by optical characterization (Supporting Information).

We further analyzed the ultrafine particles through Raman spectroscopy, with 532 nm laser excitation (Figure 1c). Two prominent peaks (339 and 378 cm<sup>-1</sup>)

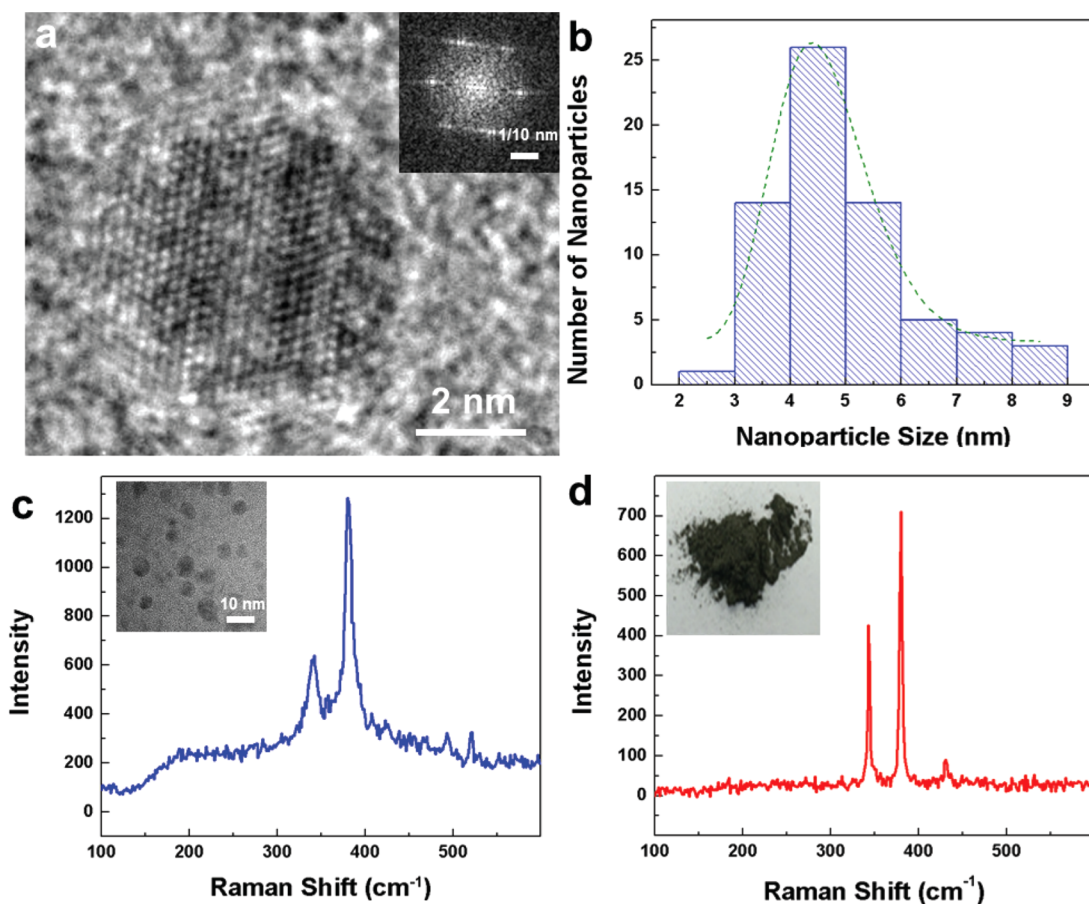


**Figure 1.** (a) Representative TEM image of synthesized FeS<sub>2</sub> nanoparticle with inset showing FFT diffraction pattern of crystalline structure; (b) particle size distribution with log-normal fit based on TEM image analysis; Raman spectra taken with 532 nm excitation for (c) ultrafine FeS<sub>2</sub> nanoparticles with SEM inset and (d) bulk FeS<sub>2</sub> powder with inset of image of purchased powder.

are observed that are indicative of the presence of S–S bonds and agree with other literature reports of nano-scale FeS<sub>2</sub> materials.<sup>5,6</sup> The stretch mode observed near 339 cm<sup>-1</sup> is due to displacement of S atoms perpendicular to the S–S bond ( $E_g$ ), and the mode near 378 cm<sup>-1</sup> is due to in-plane S–S stretching vibrations ( $A_g$ ). A third peak that we attribute to the  $T_g$  symmetry mode is also visible at ~420 cm<sup>-1</sup>. The absence of peaks around 210 and 280 cm<sup>-1</sup> confirms the absence of FeS in the synthesized sample. Likewise, the absence of Raman peaks around 386 and 323 cm<sup>-1</sup> indicates a lack of marcasite, orthorhombic FeS<sub>2</sub>, and confirms the synthesized structure of pyrite FeS<sub>2</sub>.<sup>6</sup> The Raman spectra of the ultrafine FeS<sub>2</sub> are compared to bulk FeS<sub>2</sub> (Figure 1d), as our study uses bulk FeS<sub>2</sub> material as a benchmark to compare and understand the role of ultrafine nanostructuring on the observed performance and material characteristics. The Raman peaks from the bulk FeS<sub>2</sub> powder match well with those of the nanoparticles and are shifted ~3 cm<sup>-1</sup> due to the difference in surface to bulk ratios. Size distributions of the bulk FeS<sub>2</sub> materials based on SEM analysis (Figure S3) indicate a distribution peaked near ~1  $\mu$ m, with an average particle size of ~1.9  $\mu$ m.

To assess the electrochemical performance of FeS<sub>2</sub> nanoparticle devices, we combined FeS<sub>2</sub> ultrafine nanoparticles, carbon black, and PVDF into a slurry and cast it onto a stainless steel electrode. This electrode was combined with either sodium or lithium electrodes, pressed into a coin cell, and tested in a half-cell configuration with either NaPF<sub>6</sub>/DGM or LiPF<sub>6</sub>/EC-DEC electrolytes for sodium ion and lithium ion cells, respectively. Whereas our primary focus is on sodium ion batteries, we performed a series of experiments comparing ultrafine nanoparticles and bulk FeS<sub>2</sub> powder electrodes in the context of both sodium ion and lithium ion batteries to understand the general effect of ultrafine particles on both observed conversion reactions.

The sodium and lithium storage behavior of FeS<sub>2</sub> ultrafine nanoparticles was assessed through both cyclic voltammetry (CV) and galvanostatic cycling experiments, with comparison to electrodes composed of bulk FeS<sub>2</sub> electrode materials (Figure 2). In all cases, CV curves were recorded at a constant rate of 0.1 mV/s, starting from the open circuit voltage and cycling between 0.001 and 3 V vs Na/Na<sup>+</sup>. The first, second, and third CV cycles for both bulk powder (Figure 2a,b)

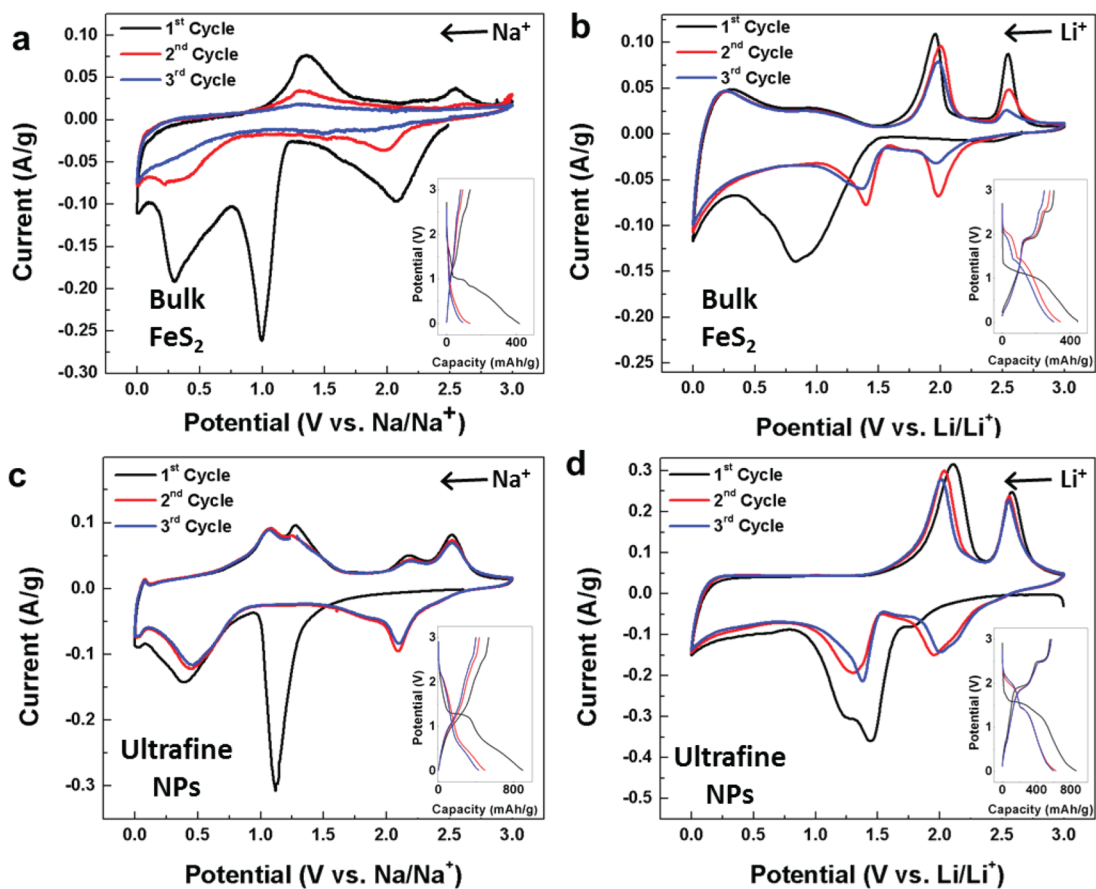


**Figure 2.** Electrochemical characterization of Na-FeS<sub>2</sub> and Li-FeS<sub>2</sub> cells. Cyclic voltammetry (CV) at 0.1 mV/s scan rates for (a) bulk FeS<sub>2</sub> Na<sup>+</sup> cells, (b) bulk FeS<sub>2</sub> Li<sup>+</sup> cells, (c) ultrafine FeS<sub>2</sub> nanoparticle Na<sup>+</sup> cells, and (d) ultrafine FeS<sub>2</sub> nanoparticle Li<sup>+</sup> cells. In all cases, the first three insertion-extraction cycles are shown and galvanostatic charge-discharge data for the first, second, and third cycles at 0.1 A/g are inset.

and nanoparticle devices (Figure 2c,d) are shown with corresponding galvanostatic charge-discharge curves inset. For Na-FeS<sub>2</sub> devices (Figure 2a,c), we observe three evident Na<sup>+</sup> insertion peaks for bulk powders near 2.1, 1, and 0.25 V and two peaks for ultrafine nanoparticle devices near 1.1 and 0.4 V. Subsequent Na<sup>+</sup> extraction occurs through a series of two peaks in both cases, near 1.25 and 2.25 V. We infer these peaks are due to Na<sup>+</sup> intercalation at high voltages to form Na<sub>x</sub>FeS<sub>2</sub> ( $x < 2$ ), then subsequent conversion at lower voltages to form Fe + Na<sub>2</sub>S.<sup>31,34</sup> This is in turn reversed in a similar manner through the reaction of Fe + Na<sub>2</sub>S at lower voltages to form Na<sub>2</sub>FeS<sub>2</sub> and the removal of sodium at higher voltages to form Na<sub>2-x</sub>FeS<sub>2</sub> ( $0 < x < 2$ ). In both cases, the peak near 1 V is irreversible and precedes a lower voltage conversion transformation. Inset galvanostatic charge-discharge curves taken at 0.1 A/g for first, second, and third cycles indicate similar features to the CV curves, with reversible capacities near 500 mAh/g for nanoparticles and 300 mAh/g for bulk powders. Notably, first discharge profiles also indicate irreversible capacity in both cases that we attribute to initial intercalation and SEI formation that precede the conversion process. Additionally, CV

curves shown in Figure 2a for bulk electrodes exhibit significant degradation of all peaks after three CV scans at slow scan rates of 0.1 mV/s, leading to a capacitive storage signature, whereas the FeS<sub>2</sub> ultrafine nanoparticles exhibit excellent stability of observed conversion reaction peaks over three cycles. This supports a consistent theme of this work that elucidates the reversible cycling in ultrafine nanoparticles and irreversible processes in bulk powder electrodes. Notably, the trends observed for Li<sup>+</sup> insertion and extraction mirror that of Na<sup>+</sup> (Figure 2b,d), except with a conversion reaction that produces Fe + Li<sub>2</sub>S<sup>6,29,31,41-44</sup> through an intercalation process to form Li<sub>2-x</sub>FeS<sub>2</sub> ( $0 < x < 0.8$ ) (~2.6 V),<sup>6,27,34,45</sup> which is reversed in a similar manner to that observed with Na<sup>+</sup>.<sup>5</sup> CV curves taken in a more focused voltage window of 1–3 V are shown in Figure S4. Further, similar to that observed for Na<sup>+</sup> devices, CV curves indicate compromised cycling performance over three CV cycles for bulk electrodes and reversible redox conversion storage over three CV cycles for ultrafine nanoparticles.

Whereas the clear differentiation between cyclability in bulk electrode materials and ultrafine NPs is evident in Figure 2, cycling and rate capability studies on all

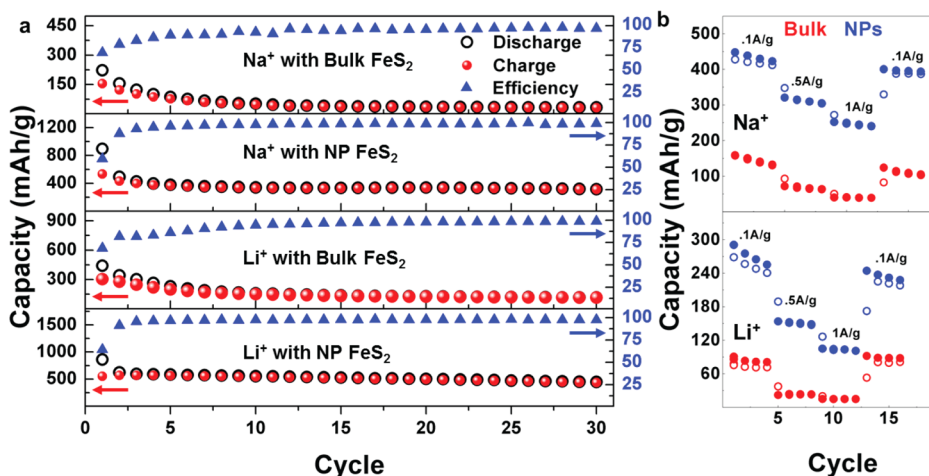


**Figure 3.** (a) Cycling performance and charge efficiency of bulk and ultrafine nanoparticle devices in Na–FeS<sub>2</sub> and Li–FeS<sub>2</sub> cell configurations, using galvanostatic cycling at 0.1 A/g, and (b) performance of devices with higher galvanostatic charge–discharge rates for Na<sup>+</sup> and Li<sup>+</sup> devices.

samples were performed for sodium ion and lithium ion cells and are presented in Figure 3. A characteristic feature of bulk FeS<sub>2</sub> cycling is a rapid loss of capacity in the first few cycles, accompanied by poor charge efficiency, not as apparent for ultrafine NPs. Additionally, in both cases the ultrafine NP cycling performance stabilizes, whereas the bulk cycling performance consistently declines over 30 cycles. For Na<sup>+</sup> cells, we observe ultrafine NP electrodes to exhibit 64% of the initial discharge capacity (relative to second cycle) over 30 cycles, with only a 6% decline of capacity between cycle 10 and 30, indicating stable cycling performance. This is compared to bulk electrodes, which exhibit a 79% total loss (maintaining only 21% of the second cycle capacity) in capacity over cycling, with 36% capacity loss in the last 20 cycles. Notably, this trend also holds for Li<sup>+</sup> cells, where the ultrafine NP electrodes maintain 72% of initial (second cycle) capacity after 30 cycles, whereas bulk electrodes only retain 34%. As expected, the Na<sup>+</sup> cells indicate a more significant divide between cycling performance of ultrafine NP electrodes and bulk material electrodes due to the larger size of Na ions. Additionally, these trends hold for rate capability studies (Figure 3B), where cycling up to 1 A/g was achieved. Due to SEI formation in the first cycle that precedes a chemical transformation occurring in subsequent cycles rate-limited by the mass diffusion of Fe in FeS<sub>2</sub> ( $L_D \approx 10^{-18} \text{ cm}^2 \text{ s}^{-1}$ ), the bulk materials exhibit virtually negligible capacity at higher rates of 1 A/g in both cases, whereas the ultrafine FeS<sub>2</sub> NPs exhibit stable capacities of >250 and >100 mAh/g for both Na<sup>+</sup> and Li<sup>+</sup> cells cycled at 1 A/g, respectively. This provides support for good rate capability that is enabled by short Fe diffusion lengths in the ultrafine nanocrystals. Furthermore, it is important to note that an absolute comparison of capacity in our FeS<sub>2</sub> ultrafine NP electrodes relative to other reports utilizing intermediate-sized nanostructures (e.g., 40–50 nm)

indicates results that are in some cases slightly improved<sup>34</sup> or in other cases slightly lower.<sup>6</sup> However, given the importance of size-limited mass diffusion occurring during cation-exchange processes, it is important to design experiments to decouple (i) fundamental size- or shape-dependent characteristics of these processes and (ii) properties at the device level that are related to electrode processing. In this manner, the comparison between ultrafine NPs and bulk particles presents a size comparison extreme enough to clearly distinguish the difference in size on this cation-exchange process.

At this point, electrochemical analysis indicates a consistent picture where ultrafine FeS<sub>2</sub> NPs outperform bulk FeS<sub>2</sub> electrode materials on all fronts of capacity, cyclability, and rate capability, but mechanistic understanding differences in these two electrode materials remain elusive. We therefore performed both *ex-situ* scanning transmission electron microscopy energy dispersive X-ray spectroscopy (STEM EDS) analysis (Figure 4) and *ex-situ* Raman spectroscopic analysis (Figure 5) to understand the mechanistic role that ultrafine NPs play to enable this improved performance. In both cases we focused our efforts on Na ion cells because in this system the ultrafine FeS<sub>2</sub> NP electrodes exhibit the greatest benefit toward cycling and rate capability in comparison to bulk FeS<sub>2</sub> electrodes. In the first case, we performed STEM analysis on FeS<sub>2</sub> electrodes after two subsequent charge–discharge cycles in Na<sup>+</sup> cells. Shown in Figure 4a is a representative STEM EDS map of cycled FeS<sub>2</sub> nanocrystals that contain multiple FeS<sub>2</sub> ultrafine NPs. The cluster contains a uniform distribution of Na, Fe, and S elements evenly distributed throughout the material, indicative of the formation of a uniform chemical conversion process that occurs throughout the material. Individual EDS maps further support sodium distribution through the cluster of ultrafine NPs, indicating that Fe diffusion out of the sulfur anion sublattice and cation-exchange with

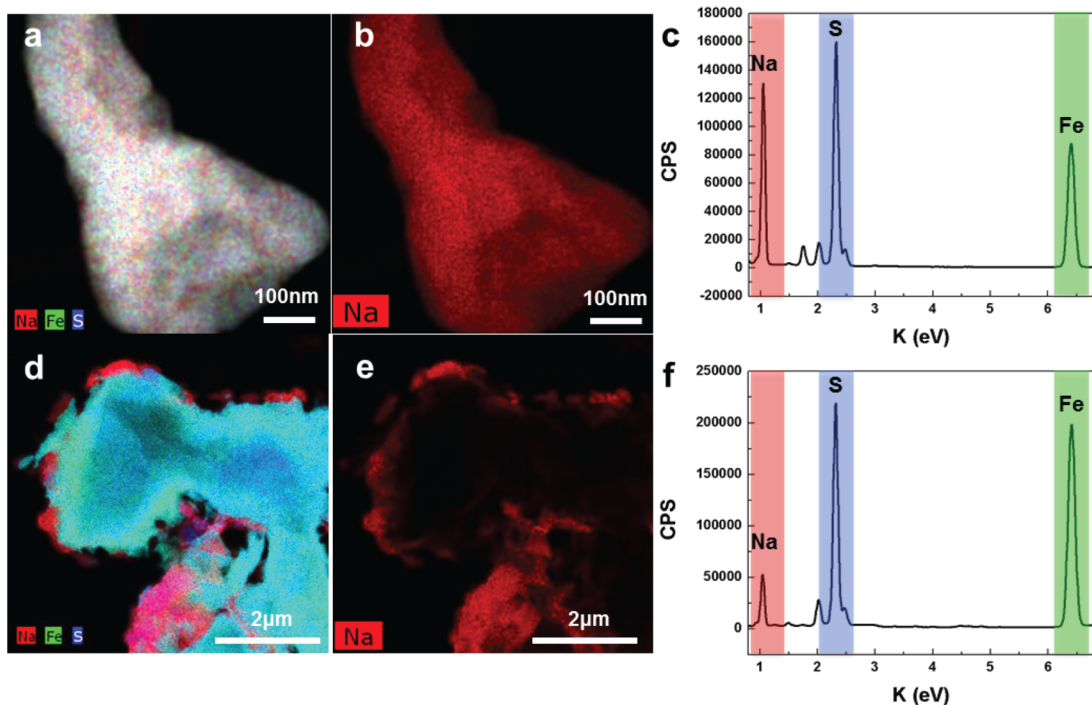


**Figure 4.** (a) STEM EDS map taken after sodium insertion of an agglomerate of NPs; (b) Na isolation in the same agglomerate; (c) X-ray spectra of NPs; (d) STEM map of bulk powder; (e) Na-only map of image in (d); and (f) elemental spectra of bulk powder.

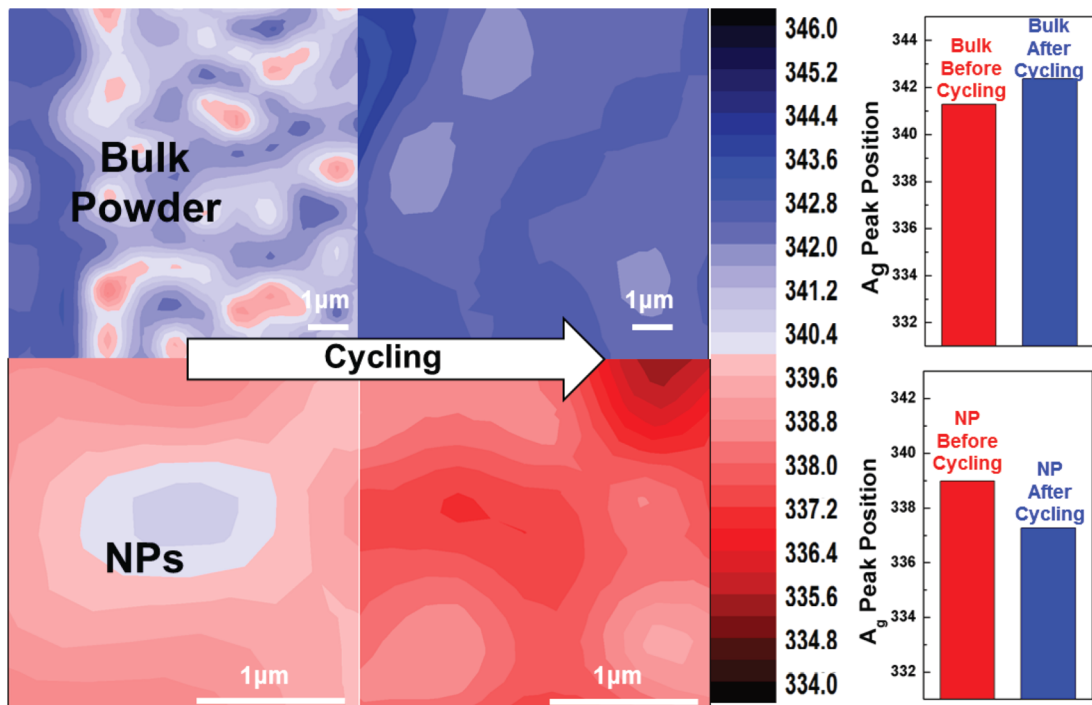


**Figure 5.** Raman spectroscopic mapping of the A<sub>g</sub> peak in bulk FeS<sub>2</sub> (top) and ultrafine FeS<sub>2</sub> NPs (bottom) after cycling in a Na–FeS<sub>2</sub> cell configuration. Each map is a compilation of >200 independent Raman scans. (Right) Average position of the A<sub>g</sub> peak based on data in maps.

Na uniformly occur throughout the structure. Comparing the X-ray spectra obtained from EDS maps (Figure 4c), the ratio of Na/Fe is 1.48.

On the other hand, the EDS maps of flakes containing bulk FeS<sub>2</sub> materials after two cycles tell a different

story, where the conversion products are not uniformly distributed through the material, and separate domains containing Na and FeS<sub>2</sub> can be identified (Figure 4d), with an elemental Na/Fe ratio of 0.26. Separate EDS maps (Figure 4e) indicate that sodium

conversion products are produced only near the surface of the bulk material flake, leaving the interior material in the flake unreacted. Also apparent from the composite EDS map is Fe-rich domains and a slight elemental concentration gradient between the interior and exterior of the bulk flake. Collectively, these two observations immediately highlight a marked difference in the mechanistic nature of the storage processes in ultrafine nanoparticles and bulk materials.

To further support the TEM analysis, we performed *ex-situ* Raman spectroscopic mapping of both bulk and ultrafine NP  $\text{FeS}_2$  electrodes after two charge–discharge cycles (Figure 5). Each map is a compilation of >200 individual Raman spectroscopic scans over an area from tens (NPs) to hundreds (bulk) of micrometers. To analyze the effect of  $\text{Na}^+$  cycling in these materials, we studied the position of the  $A_g$  mode that corresponds to S–S stretch modes occurring normal to the in-plane  $\text{FeS}_2$  S–S bond configuration. As  $\text{Na}^+$  enters into the pyrite structure along the (111) direction,<sup>31</sup> the  $\text{Na}^+$  intercalates between the S layers and converts the material from  $\text{FeS}_2$  to  $\text{Fe} + \text{Na}_x\text{S}$ , yielding a shift in the  $A_g$  peak position. In the case of bulk electrodes, we observe an average (statistical) blue shift of  $\sim 1 \text{ cm}^{-1}$ , whereas for ultrafine NP electrodes, we observe an average red shift of  $\sim 2 \text{ cm}^{-1}$ . This indicates a greater absolute effect of Na interaction with ultrafine NPs relative to bulk consistent with greater capacity measured in electrochemical data (Figure 2) and elemental scans of Na in *ex-situ* TEM (Figure 4). Second, the observation of blue-shifted (bulk) *versus* red-shifted (NP) modes averaged from statistically relevant maps indicates a different physical environment in the electrode materials following cycling. In the case of bulk electrodes, a blue shift can be interpreted as a compressive strain that is imposed on normal S–S stretch modes,<sup>46</sup> likely due to the formation of irreversible surface-bound products that remove Fe cations from the  $\text{FeS}_2$  bulk, yielding vacancy-mediated uniform compressive stress on the  $\text{FeS}_2$  crystal. However, in the case of ultrafine NPs, we observe oppositely red-shifted  $A_g$  modes, which indicate expansion-related stresses on unconverted  $\text{FeS}_2$ . As remaining, unconverted  $\text{FeS}_2$  will exist in close proximity to converted products, these stresses are anticipated to arise from nanoscale interfaces between converted  $\text{Na}_x\text{S}$  and  $\text{FeS}_2$ , as the unit cell for  $\text{Na}_x\text{S}$  is larger than  $\text{FeS}_2$  ( $a = 0.652 \text{ nm}$  for  $\text{Na}_x\text{S}$  *versus*  $a = 0.542 \text{ nm}$  for  $\text{FeS}_2$ ).<sup>47</sup> These conversion products pinned directly at strained interfaces of unconverted materials offer a rapid kinetic pathway for complete conversion or efficient reversal transformations. This is in contrast to flakes of bulk electrode materials, where conversion products are isolated at the electrode–electrolyte surface, requiring conversion and reversal processes mediated by atomic diffusion, both observations in agreement with *ex-situ* TEM analysis.

A picture therefore emerges that emphasizes the advantageous properties of ultrafine NPs in Na–(or Li–)sulfur conversion reactions, which is generally illustrated schematically in Figure 6. In comparison to alloying or intercalation reactions where metal ions simply shuttle in and out of host storage materials, conversion reactions involve the chemical transformation of a host lattice into products that must be kinetically and thermodynamically accessible to achieve reversibility. For bulk  $\text{FeS}_2$  electrode materials, where the diffusion length of Fe during the cation-exchange reaction is orders of magnitude smaller than the size of the bulk crystallite,<sup>19</sup> chemical conversion processes are confined to the surface of the crystallite and mediated by the diffusion of both Fe and S species to the surface from the crystallite interior. This leads to 100–500 nm sized clusters of  $\text{Na}_x\text{S}$ , as evidenced by TEM (Figure 4) and the formation of Fe-rich domains where Fe diffusion can occur only from a limited distance from the surface of the particle. The concentration gradient from unconverted but Fe-depleted  $\text{FeS}_2$  results in an  $\text{FeS}_x$  crystallite under vacancy-induced compressive strain (Figure 5) and kinetic barriers toward reverse chemical transformations. As large  $\text{Na}_x\text{S}$  conversion products and Fe-rich domains form on the surface to minimize the Gibb's free energy, these domains require greater energy over longer times to overcome entropic barriers for reversal. This is consistent with the first extraction peak positions observed in CV scans (Figure 2), which indicate a greater overpotential for bulk powder electrodes and an increase in overpotential for bulk electrode  $\text{Li}^+$  cells upon successive cycling between the second and third cycles. This is in contrast to ultrafine nanoparticles, where the overpotential decreases with cycling in all cases (see Supporting Information Figures S6 and S7). This indicates that stable conversion products and long diffusion lengths for reversal ultimately present barriers toward stable, reversible cycling. Simply nanostructuring the electrode material—an approach effective for intercalation or alloying reactions—does not necessarily overcome these constraints since the Fe diffusion length during the cation-exchange reaction remains a limiting factor until the  $\text{FeS}_2$  nanoparticles achieve length scales less than  $\sim 10 \text{ nm}$  based on previous insight from *in-situ* TEM measurements. This is notably a size regime where SEI layer effects dominate, and most often prohibit, performance in intercalation or alloying storage reactions. However, we argue that ultrafine  $\text{FeS}_2$  NPs provide clear mechanistic advantages in this regime. First, due to the short diffusion length of Fe during cation exchange, Fe and  $\text{Na}_x\text{S}$  form domains that maintain short separation distances due to the pinning of Fe species near conversion products. This is evidenced through *ex-situ* TEM and through *ex-situ* Raman analysis that indicates tensile strain in unconverted  $\text{FeS}_2$  for ultrafine NPs, an

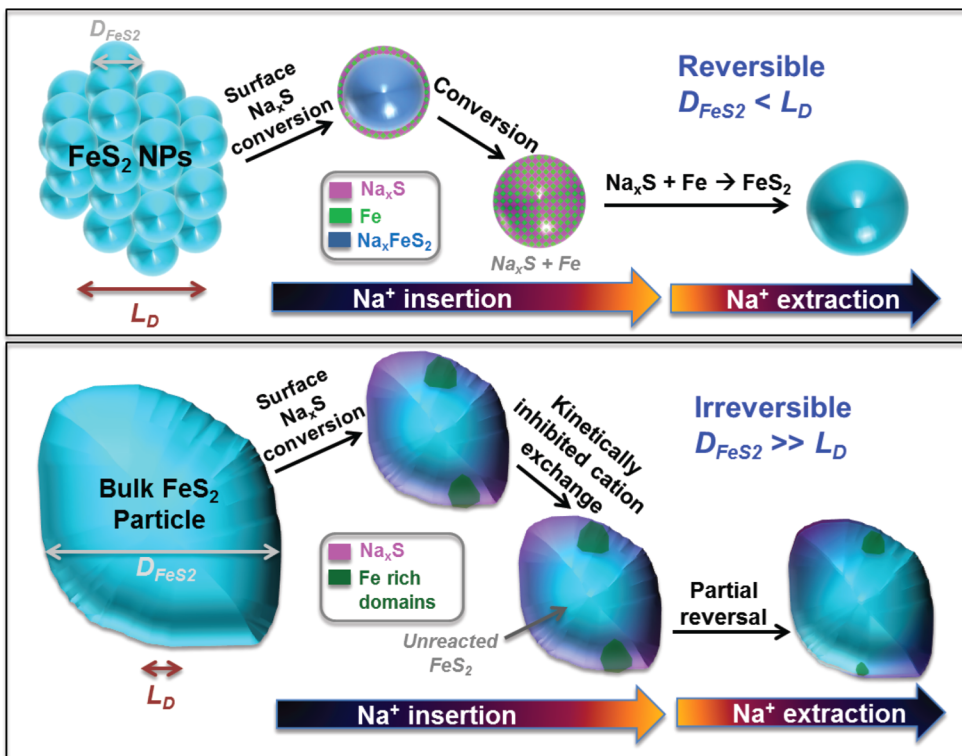


**Figure 6.** Scheme illustrating the benefit of using ultrafine NPs in sodium–sulfur conversion systems and the kinetic and thermodynamic limitations that make cycling of bulk electrode materials irreversible and ultrafine nanoparticles reversible.  $L_D$  corresponds to the diffusion length of Fe ions to perform cation exchange, and  $D_{FeS2}$  is the diameter of the  $FeS_2$  bulk or nanoparticle.

effect that can occur only for strained interfaces in nanoscale domains. This means that reversal reactions are kinetically accessible, unlike storage in bulk  $FeS_2$ . Previous reports have elucidated the necessity for ultrafine sizes in cation-exchange processes with CdSe nanocrystals,<sup>48</sup> even though such concepts have never been applied to storage reactions in battery systems. Second, the conversion products form at length scales comparable to the ultrafine NPs, compared to length scales of hundreds of nanometers for bulk materials. This means that the high free energy from ultrafine conversion domains minimizes the entropic barrier for reversal, yielding lower overpotentials and thermodynamic properties that facilitate reversible cycling. Overall, this presents a design route for electrode materials undergoing chemical conversion reactions where *rational* nanostructuring is a powerful tool to produce electrode structures that can store and release energy without adverse effects from size- and potentially shape-dependent kinetic and thermodynamic constraints.

## CONCLUSION

We demonstrate that ultrafine  $FeS_2$  nanoparticles bring mechanistic advantages for batteries that store charge through chemical conversion reactions. Electrochemical characterization of ultrafine  $FeS_2$  NPs compared to bulk  $FeS_2$  materials indicates improved

capacity, improved cycling, and better rate capability for  $FeS_2$  NPs. *Ex-situ* TEM and Raman data for Na– $FeS_2$  cells indicate this improvement is due to overcoming the significant kinetic and thermodynamic constraints of chemical conversion that is based upon a particle size comparable or smaller than the Fe diffusion distance during cation exchange and the formation of pinned nanoscale converted domains that facilitate chemical reversal. These limiting mechanisms for sodium–sulfur and lithium–sulfur conversion processes are more complex than alloying or intercalation storage reactions widely studied for metal-ion batteries and specifically highlight the benefit of ultrafine or quantum dot length-scale nanoparticles for reversible and efficient storage. Not only does this provide a route to match low-cost materials with high-capacity sodium–sulfur (or lithium–sulfur) based conversion storage reactions, but it opens up a pathway toward a new size regime for the design of chemical storage systems. As a significant effort has been placed on understanding the manifestation of quantum mechanical phenomena in nanocrystals and quantum dots toward applications in recent years, we anticipate an exciting research area existing at the intersection of quantum-confined nanostructures and energy storage or conversion processes where kinetics and thermodynamics ultimately dictate performance. This is compounded by our results that demonstrate, for the first

time, that mechanistic processes occurring during sodium–sulfur and lithium–sulfur chemical conversion

reactions are enhanced by nanostructures that have features at this length scale.

## METHODS

**FeS<sub>2</sub> Synthesis.** Iron(II) chloride tetrahydrate ( $\text{FeCl}_2 \cdot 4\text{H}_2\text{O}$ , 99%), sodium thiosulfate pentahydrate ( $\text{Na}_2\text{S}_2\text{O}_3 \cdot 5\text{H}_2\text{O}$ , 99.5%), thioglycolic acid (TGA, 99%), and anhydrous ethanol were purchased from Sigma-Aldrich. E-pure deionized water ( $18.2 \text{ M}\Omega \cdot \text{cm}$ ) was obtained from a Millipore Milli-Q system. All chemicals were used as received without any further purification. In a typical synthesis following a method previously described and modified from Bai *et al.*,<sup>39</sup> 0.123 g (1.15 mmol) of  $\text{FeCl}_2 \cdot 4\text{H}_2\text{O}$  was dissolved in 45 mL of dimethyl sulfoxide (DMSO) and 180  $\mu\text{L}$  (2.60 mmol) of TGA. This solution was placed in a three-necked flask fitted with a valve and was deaerated by bubbling of 99.99% nitrogen for 30 min. A second solution of 0.725 g (2.93 mmol) of  $\text{Na}_2\text{S}_2\text{O}_3 \cdot 5\text{H}_2\text{O}$  (Aldrich) in 10 mL of 18 MΩ deionized water under a  $\text{N}_2$  atmosphere was dissolved under a nitrogen atmosphere and dropwise added into the solution while stirring and continuously purging the reaction media with nitrogen for 15 min. The nanoparticles were allowed to grow and crystallize under conditions of continuous reflux at 139 °C for 4 h. Upon completion, the NPs were separated from the reaction media by centrifugation and purified several times with methanol. The final products were dried under vacuum at 60 °C for 6 h and stored under an Ar atmosphere. Pictures of the reaction at each stage are shown in the Supporting Information.

**Sodium Ion and Lithium Ion Battery Device Fabrication and Electrochemical Testing.** Half-cell devices were assembled in an Ar glovebox using 2032 stainless steel coin cells (MTI). For the sodium ion batteries, the FeS<sub>2</sub> NPs were dispersed in a slurry with conductive carbon black and PVDF binder at a ratio of 3:1:1, respectively. The slurry is assembled as a cathode material with a 2500 Celgard separator saturated with 1 M NaPF<sub>6</sub> in diethylene glycol dimethyl ether (DGM) (Sigma-Aldrich) separating the cathode material from pure sodium foil (Sigma-Aldrich). The same procedure is followed for the lithium ion batteries, using lithium (Sigma-Aldrich) as the counter electrode and, for the electrolyte, 1 M LiPF<sub>6</sub> in 1 g/1 mL of ethylene carbonate (EC) and diethyl carbonate (DEC). The devices were tested utilizing a Metrohm Autolab multichannel testing system. Cyclic voltammetry was performed at room temperature on the devices between 0 and 3.0 V at a constant scan rate of 0.1 mV/s, and galvanostatic charge–discharge measurements were carried out for constant currents ranging from 0.1 to 1 A/g. Cycling studies were performed at 0.1 A/g.

**Ex-Situ TEM and Raman Analysis.** Batteries were cycled twice and left in a fully sodiated state to characterize products of sodiation. For TEM analysis, electrode materials from disassembled coin cells were scraped onto amorphous carbon TEM grids inside the Ar glovebox and subsequently imaged using an FEI Osiris TEM at a beam voltage of 200 kV and a screen current of 1.3 nA. For Raman spectroscopic preparation, electrodes from disassembled coin cells were placed between two glass slides with an O-ring around the steel disc inside the Ar glovebox. The sides of the glass slides were clamped with binder clips, and the airtight system was then utilized for ex-situ Raman experiments. Raman measurements were performed on a Renishaw inVia microscope using 532 nm laser excitations.

**Conflict of Interest:** The authors declare no competing financial interest.

**Acknowledgment.** We thank Andrew Westover, Nitin Muralidharan, and Mengya Li for their discussions related to batteries, and Rizia Bardhan for useful discussions about nanoparticle synthesis. This work was supported in part by National Science Foundation grant EPS 1004083 and Vanderbilt start-up funds. A.D., A.P.C., and K.S. are supported in part by the National Science Foundation Graduate Research Fellowship under Grant No. 1445197.

**Supporting Information Available:** The Supporting Information is available free of charge on the ACS Publications website at DOI: 10.1021/acsnano.5b04700.

Photographs and description of wet-chemical synthesis of FeS<sub>2</sub>, UV–vis characterization of synthesized nanoparticles, distribution of bulk FeS<sub>2</sub> particle sizes based on SEM analysis, CV curves of devices cycled in focused voltage ranges, table of observations in previously studied ultrafine NPs in conversion/nonconversion reactions, and visual analysis of CV curves to analyze changes in overpotential in the FeS<sub>2</sub> electrodes (PDF)

## REFERENCES AND NOTES

1. Arico, A. S.; Bruce, P.; Scrosati, B.; Tarascon, J. M.; van Schalwijk, W. Nanostructured Materials for Advanced Energy Conversion and Storage Devices. *Nat. Mater.* **2005**, *4*, 366–377.
2. Bardhan, R.; Hedges, L. O.; Pint, C. L.; Javey, A.; Whitelam, S.; Urban, J. J. Uncovering the Intrinsic Size Dependence of Hydriding Phase Transformations in Nanocrystals. *Nat. Mater.* **2013**, *12*, 905–912.
3. Guo, Y. G.; Hu, J. S.; Wan, L. J. Nanostructured Materials for Electrochemical Energy Conversion and Storage Devices. *Adv. Mater.* **2008**, *20*, 2878–2887.
4. Bruce, P. G.; Scrosati, B.; Tarascon, J. M. Nanomaterials for Rechargeable Lithium Batteries. *Angew. Chem., Int. Ed.* **2008**, *47*, 2930–46.
5. Liu, W. L.; Rui, X. H.; Tan, H. T.; Xu, C.; Yan, Q. Y.; Hng, H. H. Solvothermal Synthesis of Pyrite FeS<sub>2</sub> Nanocubes and Their Superior High Rate Lithium Storage Properties. *RSC Adv.* **2014**, *4*, 48770–48776.
6. Li, L.; Caban-Acevedo, M.; Girard, S. N.; Jin, S. High-Purity Iron Pyrite (FeS<sub>2</sub>) Nanowires as High-Capacity Nanostructured Cathodes for Lithium-Ion Batteries. *Nanoscale* **2014**, *6*, 2112–2118.
7. Prosini, P. P.; Carewska, M.; Scaccia, S.; Wisniewski, P.; Pasquali, M. Long-Term Cyclability of Nanostructured LiFePO<sub>4</sub>. *Electrochim. Acta* **2003**, *48*, 4205–4211.
8. Li, N.; Martin, C. R.; Scrosati, B. Nanomaterial-Based Li-Ion Battery Electrodes. *J. Power Sources* **2001**, *97*, 240–243.
9. Ji, L.; Lin, Z.; Alcoutabi, M.; Zhang, X. Recent Developments in Nanostructured Anode Materials for Rechargeable Lithium-Ion Batteries. *Energy Environ. Sci.* **2011**, *4*, 2682–2699.
10. Chan, C. K.; Peng, H.; Liu, G.; McIlwrath, K.; Zhang, X. F.; Huggins, R. A.; Cui, Y. High-Performance Lithium Battery Anodes Using Silicon Nanowires. *Nat. Nanotechnol.* **2008**, *3*, 31–35.
11. Westover, A. S.; Freudiger, D.; Gani, Z. S.; Share, K.; Oakes, L.; Carter, R.; Pint, C. L. On-Chip High Power Porous Silicon Lithium Ion Batteries with Stable Capacity over 10,000 Cycles. *Nanoscale* **2014**, *7*, 98–103.
12. Li, H.; Huang, X. J.; Chen, L. Q.; Wu, Z. G.; Liang, Y. A. High Capacity Nano-Si Composite Anode Material for Lithium Rechargeable Batteries. *Electrochim. Solid-State Lett.* **1999**, *2*, 547–549.
13. Kasavajjula, U.; Wang, C.; Appleby, A. J. Nano- and Bulk-Silicon-Based Insertion Anodes for Lithium-Ion Secondary Cells. *J. Power Sources* **2007**, *163*, 1003–1039.
14. Kim, H.; Seo, M.; Park, M. H.; Cho, J. A Critical Size of Silicon Nano-Anodes for Lithium Rechargeable Batteries. *Angew. Chem., Int. Ed.* **2010**, *49*, 2146–2149.
15. Kim, C.; Noh, M.; Choi, M.; Cho, J.; Park, B. Critical Size of a Nano SnO<sub>2</sub> Electrode for Li-Secondary Battery. *Chem. Mater.* **2005**, *17*, 3297–3301.
16. He, M.; Kravchyk, K.; Walter, M.; Kovalenko, M. V. Mono-disperse Antimony Nanocrystals for High-Rate Li-Ion and

- Na-Ion Battery Anodes: Nano versus Bulk. *Nano Lett.* **2014**, *14*, 1255–1262.
17. Kravchyk, K.; Protesescu, L.; Bodnarchuk, M. I.; Krumeich, F.; Yarema, M.; Walter, M.; Guntlin, C.; Kovalenko, M. K. Mono-disperse and Inorganically Capped Sn and Sn/SnO<sub>2</sub> Nanocrystals for High-Performance Li-Ion Battery Anodes. *J. Am. Chem. Soc.* **2013**, *135*, 4199–4202.
  18. Malini, R.; Uma, U.; Sheela, T.; Ganesan, M.; Renganathan, N. G. Conversion Reactions: A New Pathway to Realise Energy in Lithium-Ion Battery—Review. *Ionics* **2009**, *15*, 301–307.
  19. McDowell, M. T.; Lu, Z.; Koski, K. J.; Yu, J. H.; Zheng, G.; Cui, Y. *In Situ* Observation of Divergent Phase Transformations in Individual Sulfide Nanocrystals. *Nano Lett.* **2015**, *15*, 1264–1271.
  20. Sun, X.; Zhou, C.; Xie, M.; Sun, H.; Hu, T.; Lu, F.; Scott, S. M.; George, S. M.; Lian, J. Synthesis of ZnO Quantum Dot/Graphene Nanocomposites by Atomic Layer Deposition with High Lithium Storage Capacity. *J. Mater. Chem. A* **2014**, *2*, 7319–7326.
  21. Song, H.; Li, N.; Cui, H.; Wang, C. Enhanced Capability and Cyclability of SnO<sub>2</sub>–Graphene Oxide Hybrid Anode by Firmly Anchored SnO<sub>2</sub> Quantum Dots. *J. Mater. Chem. A* **2013**, *1*, 7558–7562.
  22. Peng, C.; Chen, B.; Qin, Y.; Yang, S.; Li, C.; Zuo, Y.; Liu, S.; Yang, J. Facile Ultrasonic Synthesis of CoO Quantum Dot/Graphene Nanosheet Composites with High Lithium Storage Capacity. *ACS Nano* **2012**, *6*, 1074–1081.
  23. Zhou, X.; Shi, J.; Liu, Y.; Su, Q.; Zhang, J.; Du, G. Microwave Irradiation Synthesis of Co<sub>3</sub>O<sub>4</sub> Quantum Dots/Graphene Composite as Anode Materials for Li-Ion Battery. *Electrochim. Acta* **2014**, *143*, 175–179.
  24. Chen, J. H.; Harvey, W. W. Cation Self-Diffusion in Chalcopyrite and Pyrite. *Metall. Trans. B* **1975**, *6B*, 331–339.
  25. Strauss, E.; Golodnitsky, D.; Peled, E. Study of Phase Changes During 500 Full Cycles of Li/Composite Polymer Electrolyte/FeS<sub>2</sub> Battery. *Electrochim. Acta* **2000**, *45*, 1519–1525.
  26. Zhang, D.; Mai, Y. J.; Xiang, J. Y.; Xia, X. H.; Qiao, Y. Q.; Tu, J. P. FeS<sub>2</sub>/C Composite as an Anode for Lithium Ion Batteries with Enhanced Reversible Capacity. *J. Power Sources* **2012**, *217*, 229–235.
  27. Siyu, H.; Xinyu, L.; QingYu, L.; Jun, C. Pyrite Film Synthesized for Lithium-Ion Batteries. *J. Alloys Compd.* **2009**, *472*, 9–12.
  28. Wang, Y.; Liao, H.; Wang, J.; Qian, X.; Zhu, Y.; Cheng, S. Effects of Current Collectors on Electrochemical Performance of FeS<sub>2</sub> for Li-Ion Battery. *Int. J. Electrochem. Sci.* **2013**, *8*, 4002–4009.
  29. Fong, R.; Dahn, J. R. Electrochemistry of Pyrite Based Cathodes for Ambient Temperature Lithium Batteries. *J. Electrochem. Soc.* **1989**, *136*, 3206–3210.
  30. Cabana, J.; Monconduit, L.; Larcher, D.; Palacin, M. R. Beyond Intercalation-Based Li-Ion Batteries: the State of the Art and Challenges of Electrode Materials Reacting Through Conversion Reactions. *Adv. Mater.* **2010**, *22*, 170–192.
  31. Hu, Z.; Zhu, Z.; Cheng, F.; Zhang, K.; Wang, J.; Chen, C.; Chen, J. Pyrite FeS<sub>2</sub> for High-Rate and Long-Life Rechargeable Sodium Batteries. *Energy Environ. Sci.* **2015**, *8*, 1309–1316.
  32. Kim, T. B.; Choi, J. W.; Ryu, H. S.; Cho, G. B.; Kim, K. W.; Ahn, J. H.; Cho, K. K.; Ahn, H. J. Electrochemical Properties of Sodium/Pyrite Battery at Room Temperature. *J. Power Sources* **2007**, *174*, 1275–1278.
  33. Shadike, Z.; Zhou, Y. N.; Ding, F.; Sang, L.; Nam, K. W.; Yang, X. Q.; Fu, Z. W. The New Electrochemical Reaction Mechanism of Na/FeS<sub>2</sub> Cell at Ambient Temperature. *J. Power Sources* **2014**, *260*, 72–76.
  34. Walter, M.; Zünd, T.; Kovalenko, M. V. Pyrite (FeS<sub>2</sub>) Nanocrystals as Inexpensive High- Performance Lithium-Ion Cathode and Sodium-Ion Anode Materials. *Nanoscale* **2015**, *7*, 9158–9163.
  35. Golodnitsky, D.; Peled, E. Pyrite as Cathode Insertion Material in Rechargeable Lithium/Composite Polymer Electrolyte Batteries. *Electrochim. Acta* **1999**, *45*, 335–350.
  36. Yersak, T. A.; Macpherson, H. A.; Kim, S. C.; Le, V. D.; Kang, C. S.; Son, S. B.; Kim, Y. H.; Trevey, J. E.; Oh, K. H.; Stoldt, C.; et al. Solid State Enabled Reversible Four Electron Storage. *Adv. Energy Mater.* **2013**, *3*, 120–127.
  37. Wilcoxon, J. P.; Newcomer, P. P.; Samara, G. A. Strong Quantum Confinement Effects in FeS<sub>2</sub> Nanoclusters. *Solid State Commun.* **1996**, *98*, 581–585.
  38. Hueso, K. B.; Armand, M.; Rojo, T. High Temperature Sodium Batteries: Status, Challenges and Future Trends. *Energy Environ. Sci.* **2013**, *6*, 734–749.
  39. Bai, Y.; Yeom, J.; Yang, M.; Cha, S. H.; Sun, K.; Kotov, N. A. Universal Synthesis of Single-Phase Pyrite FeS<sub>2</sub> Nanoparticles, Nanowires, and Nanosheets. *J. Phys. Chem. C* **2013**, *117*, 2567–2573.
  40. Collins, T. J. ImageJ for Microscopy. *BioTechniques* **2007**, *43*, 25–30.
  41. Shao-Horn, Y. Chemical, Structural and Electrochemical Comparison of Natural and Synthetic FeS<sub>2</sub> Pyrite in Lithium Cells. *Electrochim. Acta* **2001**, *46*, 2613–2621.
  42. Shao-Horn, Y.; Osmialowski, S.; Horn, Q. C. Nano-FeS<sub>2</sub> for Commercial Li/FeS<sub>2</sub> Primary Batteries. *J. Electrochem. Soc.* **2002**, *149*, 1499.
  43. Choi, Y. J.; Kim, N. W.; Kim, K. W.; Cho, K. K.; Cho, G. B.; Ahn, H. J.; Ahn, J. H.; Ryu, K. S.; Gu, H. B. Electrochemical Properties of Nickel-Precipitated Pyrite as Cathode Active Material for Lithium/Pyrite Cell. *J. Alloys Compd.* **2009**, *485*, 462–466.
  44. Choi, J. W.; Cheruvally, G.; Ahn, H. J.; Kim, K. W.; Ahn, J. H. Electrochemical Characteristics of Room Temperature Li/FeS<sub>2</sub> Batteries with Natural Pyrite Cathode. *J. Power Sources* **2006**, *163*, 158–165.
  45. Zhang, D.; Wang, X. L.; Mai, Y. J.; Xia, X. H.; Gu, C. D.; Tu, J. P. Enhanced Electrochemical Performance of FeS<sub>2</sub> Synthesized by Hydrothermal Method for Lithium Ion Batteries. *J. Appl. Electrochem.* **2012**, *42*, 263–269.
  46. Rice, C.; Young, J.; Zan, R.; Bangert, U.; Wolverson, D.; Georgiou, T.; Jalil, R.; Novoselov, K. S. Raman-Scattering Measurements and First-Principles Calculations of Strain-Induced Phonon Shifts in Monolayer MoS<sub>2</sub>. *Phys. Rev. B: Condens. Matter Mater. Phys.* **2013**, *87*, 081307.
  47. Pearson, W. B. *A Handbook of Lattice Spacings and Structures of Metals and Alloys: International Series of Monographs on Metal Physics and Physical Metallurgy*; Pergamon Press: New York, 1958; Vol. 4.
  48. Son, D. H.; Hughes, S. M.; Yin, Y.; Alivisatos, A. P. Cation Exchange Reactions in Ionic Nanocrystals. *Science* **2004**, *306*, 1009–1012.